Effects of Uncertainty in TRMM Precipitation Radar Path Integrated Attenuation on Interannual Variations of Tropical Oceanic Rainfall

Franklin R. Robertson and Dan E. Fitzjarrald,
NASA / Marshall Space Flight Center

Christian D. Kummerow
Colorado State University

Abstract. Considerable uncertainty surrounds the issue of whether precipitation over the tropical oceans (30° N/S) systematically changes with interannual sea-surface temperature (SST) anomalies that accompany El Nino (warm) and La Nina (cold) events. Time series of rainfall estimates from the Tropical Rainfall Measuring Mission (TRMM) Precipitation Radar (PR) over the tropical oceans show marked differences with estimates from two TRMM Microwave Imager (TMI) passive microwave algorithms. We show that path-integrated attenuation derived from the effects of precipitation on the radar return from the ocean surface exhibits interannual variability that agrees closely with the TMI time series. Further analysis of the frequency distribution of PR (2A25 product) rain rates suggests that the algorithm incorporates the attenuation measurement in a very conservative fashion so as to optimize the instantaneous rain rates. Such an optimization appears to come at the expense of monitoring interannual climate variability.

1. Introduction

It is well documented that El Nino-Southern Oscillation (ENSO) events, with marked SST changes over the tropical oceans, produce significant regional changes in precipitation, water vapor, and radiative fluxes in the tropics [e.g. Ropelewski and Halpert, 1987; Lau et al., 1997; Sun and Trenberth, 2000; Curtis and Adler, 2002]. However, we still cannot yet adequately quantify the associated net integrated changes to water and heat balance over the entire tropical oceanic or land sectors, [Soden, 2000]. Robertson et al., [2001] for example, showed that substantial disagreement exists among contemporary satellite estimates of interannual variations in tropical rainfall that are associated with SST changes. Berg et al., [2002] have documented the distinct differences between precipitation structure over the eastern and western Pacific ITCZ and noted how various satellite precipitation algorithms may respond quite differently to ENSO modulations of these precipitation regimes. Resolving this uncertainty is important since precipitation and latent heat release variations over land and ocean sectors are key components of the tropical heat balance in its most aggregated form. ENSO, the most dominant coupled mode in our climate system, represents a fundamental perturbation of tropical monsoonal circulations [Palmer, 1988]. Furthermore, reproducing the regional *and* integrated relationship between SST and precipitation is an important though obviously not sufficient test of how robustly climate models treat physical processes related to climate change.

TRMM is the first satellite to carry both active and passive sensors for measuring precipitation. Each of these approaches has uncertainties associated with it. Passive estimates from the TMI are a less direct rainfall estimate since the radiometer responds to integrated liquid water, not just to raindrops. Variations in rain layer depth and influence from water vapor and surface wind variations can also complicate extracting clean interannual signals in rainfall. By comparison, the more direct measurement of hydrometeors by the TRMM PR would seem to have less uncertainty; however, the PR operates at a single frequency (13.8 GHz) so that microphysical assumptions regarding drop size distributions come into play in the process of correcting the measured reflectivity for attenuation and relating the reflectivity structure to rainfall rate.

The purpose of this paper is to document current discrepancies between various TRMM algorithms in the characterization of interannual variability (IAV) and to provide evidence that the source of this problem lies in the estimation of the rainfall attenuation correction used in the PR algorithm. Our analysis is based on the 3A25, 3B31, and 3A11 TRMM data sets which are monthly mean statistics of instantaneous retrievals (Level-2 products) gridded to five degree spatial resolution. The National Oceanic and Atmospheric Administration Operational SST products [Reynolds, 1988] are also used.

2. Salient Attributes of the 2A25 Algorithm

To facilitate discussion of the results a simplified description of the 2A25 algorithm is presented here. Details of the algorithm can be found in Iguchi and Meneghini [1994], Iguchi et. al., [2000] and in Meneghini et al., [2000]. The TRMM PR measures reflectivity $Z_m(r)$ which in turn is related to the true reflectivity, $Z_e(r)$ by the relationship

$$\frac{Z_m(r)}{Z_e(r)} = A(r) = \left[1 - 0.2\ln(10)\varepsilon \int_o^r \alpha(s) Z_m^{\beta}(s) ds\right]^{1/\beta} \quad (1)$$

The right-hand-side quantity represents an attenuation factor, A(r), which measures the fraction of signal depletion over the distance r between the radar and a range gate within the precipitating footprint. Parameters α, β and ε are related to microphysical assumptions; their values are assumed initially and modified as noted below. When the entire column from the radar to the surface is considered, the two-way path-integrated attenuation to the surface ($r = r_s$) is denoted as $PIA_{HB} = -10 \log_{10} A(r_s)$ and has units of dB. If $\varepsilon = 1.0$ then (1) corresponds to the Hitschfeld-Bordan (H-B) relationship [Hitchfeld and Bordan, 1954] which models the rainfall attenuation correction by the power law relationship involving $Z_m(r)$ in the integrand of (1). An unfortunate property of the H-B solution is that at large attenuation, A(r) approaches zero and unless the integral quantity on the right-hand-side of (1) is known to extraordinary accuracy the solution can become unstable. At high rain rates the inherent uncertainties in the quantity $\alpha(s)Z_m^{\beta}(s)$ can often yield negative values for A(r) and preclude accurate recovery of $Z_e(r)$.

One advantage of viewing rainfall from a spaceborne radar is that an alternative estimate of path-integrated attenuation, can be obtained by comparing returned power from the ocean surface in raining scenes with that from non-raining scenes [Meneghini et al., 2000]. Termed the Surface Reference Technique (SRT), this approach is formulated as

$$PIA_{SR} = \Delta\sigma^o = \langle\sigma^o_{no\text{-}rain}\rangle - \sigma^o_{rain}, \quad (2)$$

where $\langle\sigma^o_{no\text{-}rain}\rangle$ denotes the normalized radar cross-section (NSCS) in rain-free conditions for a given incidence angle away from nadir. The decrease in radar cross-section, $\Delta\sigma^o$, due principally to precipitation, is expressed in dB. With two alternative estimates of PIA, one from the H-B solution and one from changes in observed surface cross-section, the 2A25 algorithm then uses a maximum likelihood estimator (MLE) technique to derive an optimum PIA estimate. Once this estimate is obtained the parameter ε can be varied so that A(r) in (1) is consistent with the optimum PIA estimate. Because the effect of ε is to make a constant multiplicative adjustment to α, this method of accommodating the SRT estimate of PIA is termed the "alpha-adjustment method" [Iguchi and Meneghini, 1994]. At heavier rainrates where H-B estimates fail, the SRT provides accurate attenuation corrections to enable retrieval of Z_e. At very light rainrates where the H-B solution becomes most accurate, PIA_{SR} becomes noisy because the attenuation signal falls to values near inherent background variations in $\sigma^o_{no\text{-}rain}$. Alterations in α imply a change in the drop size distribution (DSD) and, in turn, changes in the associated Z_e-Rainfall relationship. Once ε is determined, parameters in the power law relationships governing attenuation, reflectivity, and rainfall rate are adjusted so that they are consistent with the implied changes in the DSD.

3. Results

The essence of the problem to be addressed here is illustrated in Fig 1. Precipitation anomaly time series are shown for three different TRMM algorithms, each representing the departures of rainfall rate averaged over the tropical oceans (30° N/S) from a monthly-resolved climatology for the period Jan 1998-July 2001. The anomalies have been normalized by the 44-month mean so that they represent fractional variations. The corresponding tropical ocean averaged SST anomalies are also presented. Both of the TMI-based passive algorithms [Wilheit et al., 1991, and Kummerow et al., 2001] exhibit a tendency toward elevated (depressed) rainfall in association with warmer (colder) SST anomalies. This is consistent with the behavior noted in other passive microwave data sets by Robertson et al., [2001]. In contrast, the TRMM PR anomalies are of weaker amplitude and have essentially no correlation with SST changes. It should be emphasized that these anomalies represent the integration of contributions by regional patterns of both positive and negative sign that possess much larger amplitudes; thus, accurate rainfall estimates are needed to avoid the effects of cancellation error.

Time series histograms of PIA_{SR} and PR rainfall offer insight as to relationship between attenuation corrections and rainfall. Figure 2a shows time series of interannual anomalies in PIA_{SR} averaged over the tropical oceans. Data at four incidence angles (0, 5, 10 and 15 degrees from nadir) available from the 3A25 data set have been averaged and scaled to account for the varying number of available monthly observations. The annual cycle for each of 30 attenuation intensity bins was computed and removed. Although somewhat noisy, the resulting pattern shows coherent interannual variations in the frequency of attenuation intensities. For example, in JFMA 1998, above average counts are found at all attenuations > 0.5 dB with a prominent maximum near 2.0 dB. Above 1.0 dB, most of 1998 (except MJJ) shows anomalously higher frequencies than succeeding years. Below about 1.0 dB the pattern behaves in an opposite sense; generally below average occurrences dominate 1998 and above average counts are found in the second half of 1999. Such a pattern is consistent with shifts in the PIA_{SR} frequency distribution to larger (1998) and smaller (1999) values. Based on analysis of σ^o data from non-raining cases, Meneghini et al., [2000] find the standard deviation (SD) of $\langle\sigma^o_{no\text{-}rain}\rangle$ over ocean to vary from about 1.2 to 3.75 dB, depending on incidence angle. The SD statistics are used as a basis for reliability estimates used in

the MLE procedure. $PIA_{SR}/SD > 3.0$ is termed reliable, $PIA_{SR} < 1.0$ is regarded as unreliable, and values falling between these limits are marginally reliable. Only SRT measurements classified as reliable or marginally reliable are included in these histogram data. While the spatial and temporal averaging in the analysis here undoubtedly reduce random noise, it is clear that attenuation values below 1.0 dB should be regarded with caution.

By integrating the occurrence anomalies of the 30 categories for each month we recover the total PIA_{SR} anomalies. Several threshold categories of PIA_{SR} have been picked as starting values: 0.01, 1.5, and 3.4 dB. Using a representative attenuation-rainfall relationship of $k = 0.024R^{1.15}$ [Meneghini et al., 2000], and assuming a rain column depth of 5 km yields values corresponding roughly to rain rate thresholds of 0.05, 5.0 and 10.0 mmh^{-1}. These calculations (Fig 2b) reveal interannual variability of PIA_{SR} that contrasts remarkably with the PR surface rainfall variations presented in Fig. 1. Whereas the 2A12 and 2A25 time series in Fig 1. correlate at only 0.12, the correlation between the 2A12 and PIA_{SR} time series using the 1.5 dB threshold is 0.75. Note that although the curve integrating over all 30 PIA_{SR} categories results in the smallest magnitude, it too is differs from the PR trace in Fig. 1.

To examine the behavior of rainfall at various intensity thresholds an analogous treatment of the PR rainfall rate frequency histograms using the 3A25 data is presented in Figs. 2c, d. The histogram data in Fig. 2c show that in contrast to the PIA_{SR} result, much of 1998 is dominated by decreased occurrences of rainfall at all rates between about 0.5 and 40 mmh^{-1}. In 1999 the anomalies largely switch sign. In Fig 2d rain rate histogram anomalies are integrated above thresholds of 5, 27, and 48 mmh^{-1}. It is clear that only for thresholds above 30 to 40 mmh^{-1} does the IAV of rain rate resemble that of the PIA_{SR}. These striking differences suggest that much of the potential influence of the PIA_{SR} is not being retained in the MLE estimation of PIA and subsequent rainfall retrievals.

Supporting evidence for the sensitivity of PR rainfall to attenuation correction also comes from considering precipitation rates at higher altitudes in rain systems where attenuation is much weaker. Ice formation and growth processes dominate rainfall production in deep convection above the freezing level [Stith et al., 2001]. Mixed phase regions in deep tropical convection are typically confined to levels warmer than -10° C with the bulk of the precipitation mass and $Z_e \geq 30$ dBZ below the freezing level (~5 km) [Petersen and Rutledge, 2001]. Thus, regions above the freezing level exhibit much lower attenuation. Figure 3 shows PR precipitation anomalies at 2, 4 and 6 km. The 4 and 6 km levels bracket the freezing level typical for tropical oceanic regions. The interannual behavior at 6 km is strikingly different from that at 2 and 4 km. Precipitation anomalies above 10% are present in early 1998 and are persistently near -5% during 1999 and early 2000. It is not yet clear to what degree the 6 km PR time series represents variations in ice mass above 6 km as opposed to interannual variations in vertical penetration of the mixed phase region with its greater reflectivity. However, a preliminary analysis of the convective / stratiform partitioning of the 6 km precipitation has shown roughly equal contributions to the interannual signal. Since stratiform precipitation at 6 km is unlikely to contain significant liquid water, the IAV cannot be explained by mixed phase variations alone. The 6 km time series bears a strong resemblance to the PIA_{SR} anomalies in Fig 2. with the correlation between the two time series at 0.80. Physically, one would expect the abundance of ice and precipitation rates at 6 km to be strongly related to attenuating rain below the freezing level since deep convection dominates contributions by warm rain processes [ref]. Because of the abundance of ice and the lack of strong reflectivities above 6 km, very little attenuation adjustment is needed and Z_e is largely independent of PIA_{SR} contributions. We can thus further infer from the strong correlation between PIA_{SR} and the PR at 6 km that any systematic interannual biases in σ^o must be rather minimal when averaged to large space and time scales and that variations in ocean surface returns are not determining the IAV in PIA_{SR}.

4. Conclusions

In summary, we have shown that at PIA values corresponding to rain rate thresholds of several mmh^{-1} and higher, the SRT method results in a signal of IAV significantly different from that of PR 2A25 algorithm for regions below the freezing level. We infer from this result that only at rain rates $\geq$ 30 to 40 mmh^{-1} is the PIA_{SR} estimate heavily weighted in the rainfall retrieval. A full explanation for why the MLE procedure for estimating PIA yields this result is still being sought; most likely it is associated with assumed relative error properties of the SRT and H-B attenuation estimates. The PIA_{SR} IAV was found to agree closely with TRMM (and other) passive microwave estimates of rainfall. Furthermore, the close agreement in IAV between PIA_{SR} and PR 2A25 precipitation at 6km where attenuation is minimal suggests that both are robust in seeing the IA signal of deep convection. Although the present results strongly support the association of higher tropical SSTs with increased precipitation, our findings should not be viewed as quantitative validation of the passive algorithms since other uncertainties remain. It must also be acknowledged that since the S/N properties of the SRT technique cannot accurately resolve attenuation at very light rain rates, it is possible that IAV of this portion of the rainfall frequency distribution differs from that of heavier rain rates. Since the PIA_{SR} is quite noisy at low rain rates, strongly weighting it in the MLE procedure would be counterproductive for some TRMM applications (e.g. data assimilation or hydrometeorological applications). Nevertheless, the PIA_{SR} constitutes the only way the PR algorithm can recognize DSD changes so finding some means of retaining this information in the PR algorithm is important for the PR to properly resolve interannual climate variations.

Acknowledgements. This work was supported by the NASA Global Water and Energy Cycle Program, the Global Precipitation Project Office, and the TRMM Science Program.

References

Berg, W, Kummerow, C and Morales, CA, 2002: Differences between east and west Pacific rainfall systems. *Accepted J. Climate.*

Sun, D-Z and KE Trenberth, 1998: Coordinated heat removal from the equatorial Pacific during the 1986-86 El Nino, *Geophys. Res. Lett.*, 25, 2659-2662.

Curtis, S and R Adler, 2000: ENSO indices based on patterns of satellite-derived precipitation. *J. Climate*, 13, 2786-2793.

Hitchfeld, W and J Bordan, 1954: Errors inherent in the radar measurement of rainfall at attenuating wavelengths. *J. Atmos. Sci.*, 11, 58–67.

Iguchi, T and R Meneghini, 1994: Intercomparison of single-frequency methods for retrieving a vertical rain profile from airborne or spaceborne radar data. *J. Atmos. Oceanic Tech.*, 11, 1507–1516.

Iguchi, T, Kozu T, Meneghini R, Awaka J, and Okamoto K, 2000: Rain-profiling algorithm for the trmm precipitation radar. *J. Appl. Meteor.*, 39, 2038–2052.

Kummerow, C, Hong, Y, Olson WS, Yang S, Adler RF, McCollum J, Ferraro R, Petty G, Shin D-B, and TT Wilheit, 2001: The evolution of the Goddard Profiling Algorithm (GPROF) for rainfall estimation from passive microwave sensors. *J. Appl. Meteor.*, 40, 1801-1820.

Lau, K-M, Wu H-T, Bony S, 1997: The role of large-scale atmospheric circulation in the relationship between tropical convection and sea surface temperature. *J Climate*, 10, 381-392.

Meneghini, R, Iguchi T, Kozu T, Liao L, Okamoto K, Jones J, and Kwiatkowski J, 2000: Use of the surface reference technique for path attenuation estimates from the TRMM precipitation radar. *J. Appl. Meteor.*, 39, 2053–2070.

Palmer, TN., Brankovic C, Viterbo P. and Miller MJ, 1992: Modeling interannual variations of summer monsoons. *J. Climate*, 5, 399-417.

Reynolds RW, 1988: A real-time global sea surface temperature analysis. *J. Climate*,1, 75-86.

Robertson, FR, Spencer RW and DE Fitzjarrald, 2001: A new satellite deep convective ice index for tropical climate monitoring: possible implications for existing oceanic precipitation data sets, *Geophys. Res. Lett.*, 28, 251-254.

Ropelewski, CF, MS Halpert, 1987: Global and regional scale precipitation patterns associated with the El Niño/Southern Oscillation. *Mon. Wea. Rev.*, 115, 1606–1626.

Soden, BJ 2000: The sensitivity of the tropical hydrological cycle to ENSO. *J. Climate*, 13, 538–549.

Stith, JL, Dye J, Bansemer A, Heymsfield A, Grainger CA, Petersen WA, and Cifelli R, 2002: Microphysical observations of tropical clouds. *J. Appl. Meteor.*, 41, 97-117.

Szoke, EJ, Zipser, EJ. and Jorgensen, DP, 1986: A radar study of convective cells in mesoscale systems in GATE. Part I: vertical profile statistics and comparison with hurricanes. *J. Atmos. Sci.*, 43, 182-198.

Wilheit TT, Chang ATC, and LS Chiu, 1991: Retrieval of monthly rainfall indices from microwave radiometric measurement using probability distribution functions. *J. Atmos. Oceanic Technol.*, 8, 118-136.

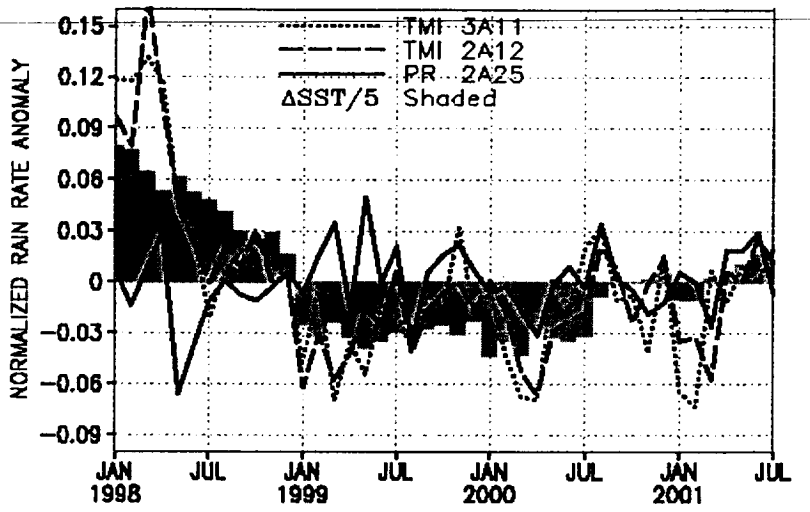

Figure 1. Time series of precipitation anomalies averaged over the tropical oceans from the TRMM PR 2A25 and passive microwave 2A12 and 3A11 algorithms. Time series have been normalized by their respective climatological values to yield fractional variability. SST anomalies over the tropical oceans scaled by 1/5 are shaded.

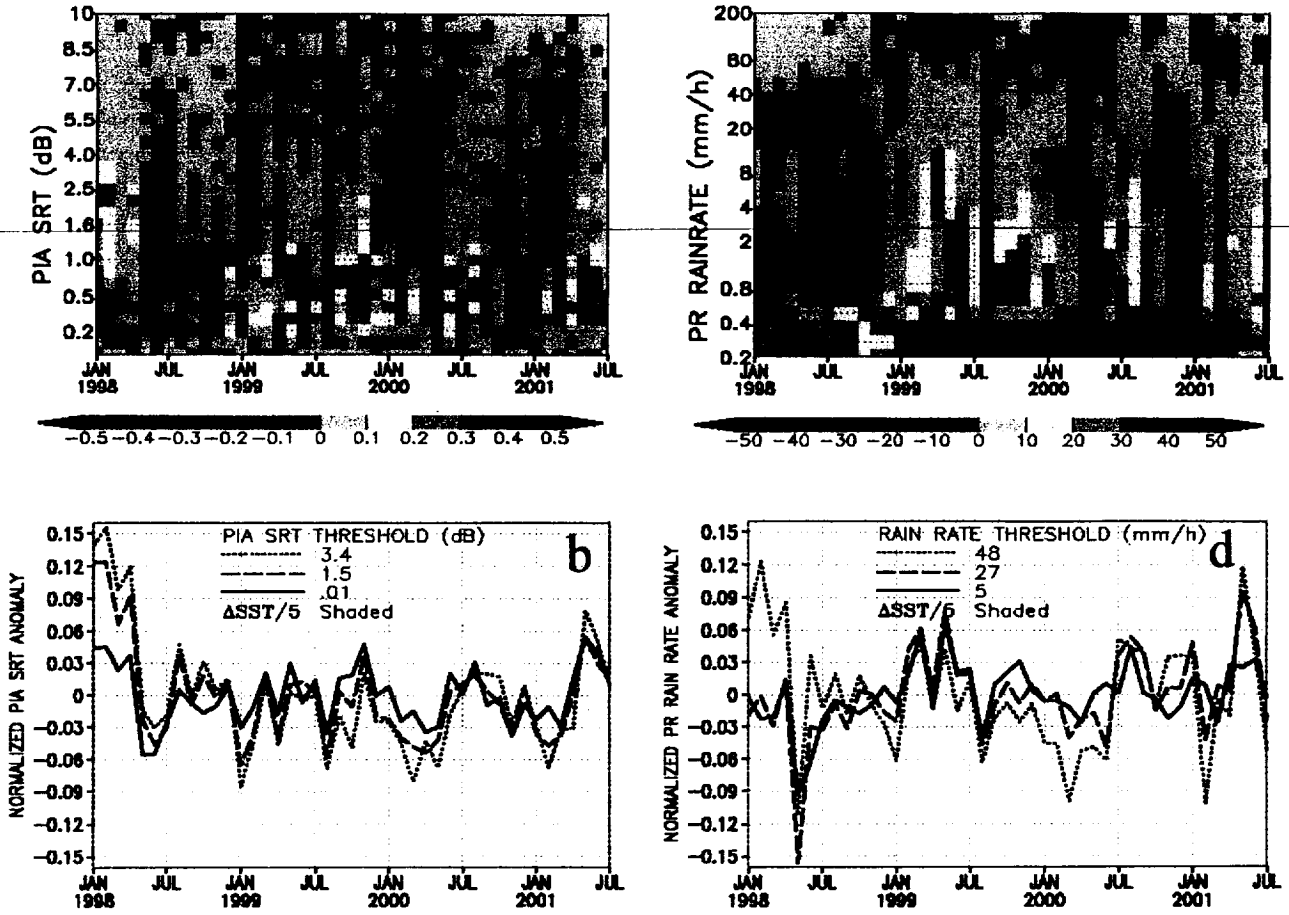

Figure 2. (a) Time series of PIA_{SR} frequency distribution anomalies averaged over the tropical oceans; (b) Anomalies of PIA_{SR} generated by integration of the frequency distribution above three intensities (.01, 1.5 and 3.4 dB); (c) Time series of PR frequency distribution anomalies averaged over the tropical oceans; (d) Anomalies of PR generated by integration of the frequency distribution above three intensities (5, 27 and 48 mmh^{-1}). Time series in (b) and (d) have been normalized by climatological values.

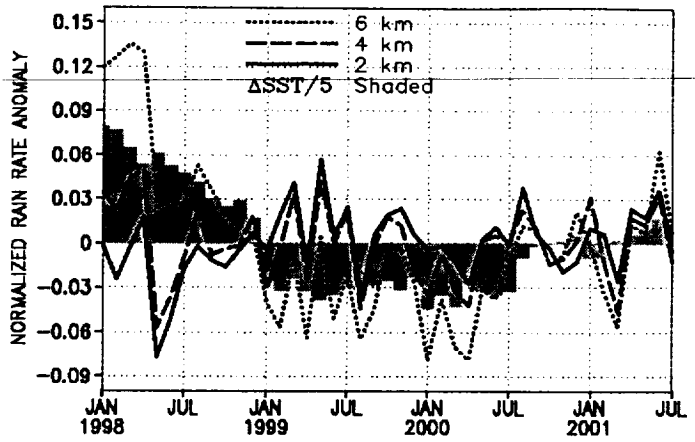

Figure 3. Time series of precipitation anomalies averaged over the tropical oceans from the TRMM PR 2A25 algorithm at the 2, 4 and 6 km levels.